Structural, magnetic, and defect properties of Co-Pt-type magnetic-storage alloys: Density-functional theory study of thermal processing effects

Aftab Alam,[1] Brent Kraczek,[2,3] and D. D. Johnson[1,2,*]

[1]*Department of Materials Science and Engineering, University of Illinois Urbana–Champaign, 1304 W. Green Street, Urbana, Illinois 61801, USA*

[2]*Department of Physics, University of Illinois, 1110 W. Green Street, Urbana, Illinois 61801, USA*

[3]*U.S. Army Research Laboratory, Aberdeen Proving Ground, Maryland 21005, USA*

(Received 18 February 2010; revised manuscript received 6 July 2010; published 30 July 2010)

Using an optimized-basis Korringa-Kohn-Rostoker-coherent-potential approximation method, we calculate formation enthalpies ΔE_f, structural, and magnetic properties of paramagnetic (PM) and ferromagnetic, disordered A1 and ordered $L1_0$ CoPt, FePd, and FePt systems that are of interest for high-density magnetic-recording media. To address processing effects, we focus on the point defects that dictate thermal properties and planar defects (e.g., *c* domain and antiphase boundaries) which can serve as pinning centers for magnetic domains and affect storage properties. We determine bulk Curie (T_c) and order-disorder ($T_{\text{o-d}}$) transition temperatures within 4% of observed values, and estimates for nanoparticles. Planar-defect energies γ_x^{hkl} show that the favorable $[hkl]$ defects depend on processing conditions as $T_c < T_{\text{o-d}}$ in these alloys, and the PM defects agree with those observed. We correlate all properties with the electronic structure.

DOI: 10.1103/PhysRevB.82.024435 PACS number(s): 75.50.Cc, 82.60.Cx, 71.15.Ap

Equiatomic, ferromagnetic (FM) $L1_0$ CoPt, FePd, and FePt (CoPt-type alloys) remain of utmost interest for ultrahigh-density magnetic-storage media,[1–4] with some promise[5] for nanometer-sized grains needed to exceed storage densities beyond 100 Gbit/in.^{2}. From their magnetic and structural properties, such as higher magnetocrystalline anisotropy energy (MAE), they are expected to have higher thermal stability for disk-drive applications. Also, the good corrosion resistance of Pt-containing $L1_0$ alloys, compared with rare-earth alloys, makes them even more attractive as media. Numerous experimental studies show that the magnetic properties of CoPt-type alloys are strongly dependent on their structural phases and on processing conditions, which often occur in the paramagnetic (PM) state because the order-disorder temperature, $T_{\text{o-d}}$, lies well above the Curie temperature, T_c, for all these alloys.[6]

After alloys are prepared from melt, vapor deposition, or solution chemistry, samples are processed below $T_{\text{o-d}}$ from magnetically soft A1 cubic phase to the hard $L1_0$ tetragonal phase,[1,2,5] where the ordering with its accompanying *c*-axis distortion yields the higher MAE. During the growth of $L1_0$ *c*-axis domains, numerous planar defects form the microstructure in the ordered phase, see Table I, e.g., *c*-domain boundaries (CDBs) and antiphase boundaries (APBs). The planar defects play an important role in the pinning of magnetic domain walls, although exact nature of this pinning is still under debate, and these defects are usually formed in the PM phase followed by annealing. While these alloys have similarities, significant differences are observed with varying processing conditions[7,8] so no prototypical behavior or microstructure exists. As such, we present results from electronic-structure calculations that account for thermal point and planar microstructural defects that must or can be present under processing conditions, address the $A1 \rightarrow L1_0$ transformation, including the effects of chemical partial long-range order (LRO) and magnetic disorder, which strongly influence the LRO, MAE, and stability of planar defects. We focus on the A_xB_{1-x} alloys at $x \approx 0.5$ with the highest MAEs.[9] We show that processing $L1_0$ alloys in their FM or PM states alters, due to differences in their electronic structure, the favorable defects that can pin magnetic domains.

The paper is structured as follows: after background on microstructure (Sec. I), we study the chemical, structural, and magnetic effects via density-functional methods (Sec. II) implemented in a multiple-scattering theory[10] [Korringa-Kohn-Rostoker (KKR)] code[11] that uses the coherent-potential approximation[12] (CPA) to address chemical and magnetic disorder. In Sec. III, along with structural and magnetic properties, we calculate formation enthalpies ΔE_f and determine phase stability as well as $T_{\text{o-d}}$ and T_c for bulk alloys and nanoparticles (NPs), with agreement to experiment. We calculate the PM and FM planar-defect energetics (e.g., $\gamma_{\text{APB}}^{hkl}$, $\gamma_{\text{CDB}}^{hkl}$, and γ_{twin}^{hkl}) and assess the defects to appear in the microstructure. These results reveal the origin of key properties, which are correlated with the electronic structure, concluding in Sec. IV.

I. MICROSTRUCTURE

For bulk alloys, $T_{\text{o-d}}$ and T_c (in kelvin), respectively, are 1100 and 720 in CoPt, 1050 and 730 in FePd, and 1600 and 750 in FePt.[6,13,14] The $T_{\text{o-d}}$ are smaller in thin films and NPs,[4,5,7] from surface and finite-size effects.[15,16] At room temperature (RT), well below T_c, FM-$L1_0$ has a large uniaxial MAE constant, due to the ordering-induced tetragonal distortion with the *c* axis (*a* axis) the easy (hard) axis, see Table I. With $T_{\text{o-d}} > T_c$, the $A1 \rightarrow L1_0$ transition typically occurs in the PM state. Unless an external field or stress is applied to break symmetry, all three *c*-axis variants must appear in the ordered phase along the A1 cube *a* axes,[17] leading to a complex hierarchic arrangement of the microstructure.[18,19] As a consequence, depending on thermal processing and related dislocation slip, the growth of $L1_0$ is

 ©2010 The American Physical Society

TABLE I. (Color online) Schematic of A1 ($c=a$) and $L1_0$ ($c \neq a$) structures and defects observed in FePd (defect planes are indicated). For each unit cell, we give the number of layers between defects used in our calculations, the number of defects m per cell, and the defect area A_{def}. Except for the (111)-twin and intrinsic stacking faults (shown with a $L1_0$ cell outlined), all others are ordering defects that reside on the parent lattice, e.g., (011) CDBs, see Fig. 1(a).

Undefected	$L1_0$ 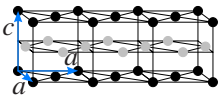	A1 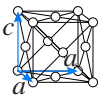
$L1_0$ Defect	Schematic	Area ($m \times A_{\text{def}}$)
(011) CDB 8 layers	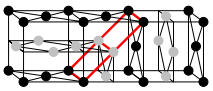	$2 \times a^2\sqrt{1+(\frac{c}{a})^2}$
(010) APB 7 layers	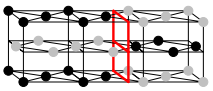	$1 \times ac$
(111) APB 6 layers	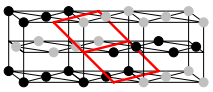	$1 \times \frac{a^2}{2}\sqrt{1+2(\frac{c}{a})^2}$
(110) APB 8 layers	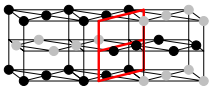	$2 \times \frac{\sqrt{2}}{2}ac$
(011) APB 8 layers	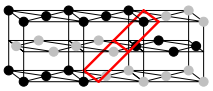	$1 \times a^2\sqrt{1+(\frac{c}{a})^2}$
(001) APB 8 layers	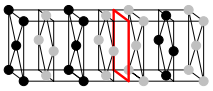	$2 \times \frac{1}{2}a^2$
(111) Twin 10 layers	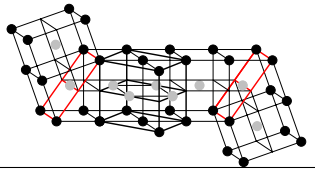	$2 \times \frac{a^2}{2}\sqrt{1+2(\frac{c}{a})^2}$
(111) ISF-1 16 layers	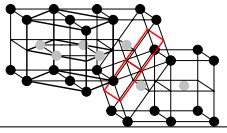	$1 \times \frac{a^2}{2}\sqrt{1+2(\frac{c}{a})^2}$
(111) ISF-2 16 layers	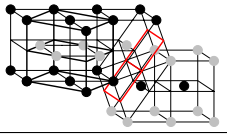	$1 \times \frac{a^2}{2}\sqrt{1+2(\frac{c}{a})^2}$

accompanied by the emergence of numerous planar defects. Micrographs for FePd and CoPt are shown in Fig. 1, with schematics of defects in Table I. The coercivity and type of defects are strongly dependent on annealing temperature and duration, often similar in "bulk" [i.e., thin transmission electron microscopy (TEM)] samples and thin-film (storage-media) samples. The current consensus is that $L1_0$'s high coercivity arises from magnetic domain-wall pinning in ordered grains, although which defects serve as pinning centers remains open.[2,3,6,13]

Although $L1_0$ is a two-atom, body-centered tetragonal cell, the bulk structures exhibit complex structures formed during ordering, and are dominated by {011} polytwins, often interspersed with APBs, see Fig. 1 and Table I, and {111} stress twins.[22] These structures are formed also in films and NPs, albeit affected by surface[15] and finite-size[16] effects. At anneal temperatures near the solvus, the $L1_0$-PM phase forms via nucleation and growth and, with the energetically favorable c-axis contraction (a and c axes forming along the a axes of the A1 parent phase), a polydomain forms to re-

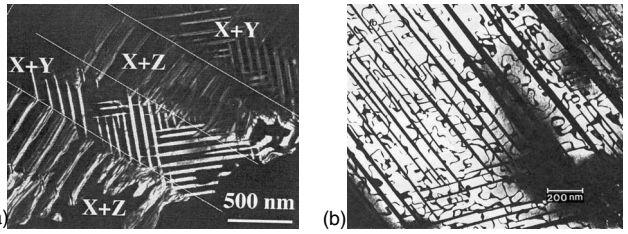

FIG. 1. Micrographs of polytwins in (a) CoPt, with two *c*-axes orientations labelled (from Refs. 20 and 21 with permission), and (b) FePd, where a high density of APBs (curvy lines) are interspersed with the parallel CDBs (from Ref. 13 with permission, Copyright Wiley-VCH Verlag GmbH & Co.). Note that intersecting CDBs are not perpendicular due to sample orientation, which is not along a *c* axis.

lieve strain energy during the transformation.[23] At small undercooling, the transformation may occur continuously, where the LRO parameter is small and grows with time; at larger undercoolings, it may occur as a massively congruent ordering.[24] So, this type of transition highly affects the microstructure.

As $L1_0$ ordering begins, stress bands form favoring growth of nuclei with specific *c*-axis orientations. When nuclei grow together, these bands form *c domains* with the same *c* axis. Strain is relieved by forming alternating domains of two of the three variants, the boundaries between *c* domains becoming {011} CDBs; the system of such CDB is called a *polytwinned* structure. The strain is relieved further by forming blocks of plates with different {011} polytwin planes, allowing all three variants to be present. Further annealing of the alloys results in a coarsening of the polytwin structure, decreasing the number of CDBs.[25] Further stress relief occurs by forming {111} twins, observed in bulk FePd (Refs. 22 and 26) and CoPt NPs.[3]

While strain favors that nuclei of a single orientation grow within a given stress band, there is no mechanism to force (001) planes of neighboring nuclei to be in phase. Thus, within a *c* domain, adjacent nuclei may have their alternating {011} planes out of phase, creating APBs, as seen in Fig. 1. In contrast to CDBs, there are no known bulk properties that influence the orientation of APBs. Thus, provided that the planar-defect energies are of similar magnitude, APBs could have any orientation, and need not form parallel planes. We will address there appearance or lack thereof in the results.

The polytwin structure is readily found and is easily seen with a light microscope after etching the surface.[27] Detailed TEM micrographs of CoPt (Refs. 20, 21, 25, and 28) and FePd (Refs. 13 and 29) are also found while for thin films and NPs, they are abundant for FePt and CoPt. The primary features in the micrographs are polytwin structures, which appear as groups of parallel lines, such as in CoPt in Fig. 1(a), Ref. 21 or FePd in Fig. 1(b).[13] APBs (the rounded, though possibly faceted, lines) are particularly prominent in the FePd micrograph,[13] absent in some CoPt micrographs[28] but possibly present in others.[25] The strain mismatch resulting from the c/a distortion in two-phase CoPt-$CoPt_3$ (with $L1_0$ and $L1_2$ phases, respectively) can lead to a *checkerboard* microstructure.[21,28,30]

Importantly, the polytwinned structure, and possibly other defect structures, significantly impact the magnetic properties of these alloys. Individual *c* domains act as magnetic *microdomains*, with magnetization parallel to the tetragonal axis and CDBs acting as microdomain walls.[6,13] The alternating *c* domains in the polytwin structure thus induce a cooperative magnetic structure, with alternating magnetic axes. Bundles of such correlated magnetic microdomains are called magnetic *macrodomains*. The high coercivity of these alloys is dependent on the pinning of the macrodomain walls as they cross bundles of *c* domains during magnetization reversal. Three different mechanisms, not mutually exclusive, have been promoted as active pinning centers for these macrodomain walls: (1) boundaries between regions of ordered and disordered alloy, (2) boundaries between different blocks of fully ordered alloy, and (3) ordering and/or structural defects with blocks of *c* domains. Of the first two options, it has been shown in FePd (Refs. 13) and in FePt and CoPt (Ref. 2) that coercivity increases until the alloys are fully ordered and that the boundaries between blocks of fully ordered alloys do pin macrodomain walls. Thus option 1 is suboptimal and option 2, which could be facilitated by pinning on CDBs between different blocks of polytwinned alloy, is definitely active. There is, however, disagreement about the role option 3 plays. Ristau *et al.*[2] observe a decrease in coercivity with annealing beyond when the alloys become fully ordered, which they attribute to the further coarsening of the polytwin structure, implying a decrease in the density of CDBs. Zhang and Soffa[13] developed a model relating the coercivity to the APB density, which would also decrease with further annealing and assumes macrodomain-wall pinning within blocks of *c* domains. However, Vlasova *et al.*[6] report having observed no such pinning within blocks of *c* domains. Thus, the relative importance of mechanisms 2 and 3 is not clear, and is likely dependent on the specific processing regimen employed. The defect energies we calculate here assist in this determination by suggesting which defects are likely to anneal out more quickly during processing.

Finally, increased storage capacity requires reducing these materials to nanometer size. This reduction in size will affect the magnetization and coercivity due to loss of chemical LRO but also structural stability relative to other morphologies. Recent calculations of the formation enthalpy of magic number NPs versus size show that multiply twinned morphologies become favored over $L1_0$ in FePt while CoPt exhibits core-shell structures.[31,32] Such core-shell behavior has a simple explanation in terms of segregation energies, and correlates with only two factors—atomic size and cohesive energy.[33] Brown *et al.*[34] have shown that FM and anti-FM states in the Invar (Ref. 35) alloy FePt are sensitive to reduction in c/a, and this behavior limits the size that is stable for high-coercivicty $L1_0$ NPs. Indeed, FePt particles below 4 nm have no LRO or T_c,[16] with similar finding in Monte Carlo simulations when considering the limit of superparamagnetism.[36] Similar behavior occurs in NP films.[37]

Thus, our calculations on bulk CoPt-type alloys with incomplete LRO and thermal effects have direct relevance to magnetic and chemical transitions and their effect on the bulk microstructures, films, and NPs.

II. COMPUTATIONAL DETAILS

Total energies were calculated from an all-electron, Green's function, density-functional theory (DFT) package developed by Johnson *et al.*,[38–40] based on KKR multiple-scattering theory[10] with the CPA (Ref. 12) to treat disorder. Core states are treated fully relativistically while valence states are handled in the scalar-relativistic approximation of Koelling and Harmon[41] in which Darwin and mass-velocity terms are included but not spin orbit. For disordered cases, we use the screened-CPA (Ref. 40) to incorporate more properly the metallic screening due to charge correlations in the local chemical environment and predict more accurate enthalpies and charges. The CPA is used to address the PM state via a disorder local moment (DLM) state,[35,42] which ignores magnetic short-range order (SRO). That is, the local site-magnetization M_i is homogeneously disordered in 4π steradians and then projected onto the global quantisation axis with site probability $1-x$ for *up* or x for *down* orientations. For a PM state $x=1/2$, for a partially FM state $0<x<1/2$ and for a fully FM state $x=0$. Note that the PM state has local moments in contrast to a nonmagnetic state.

We include s, p, d, and f symmetries, i.e., the KKR Green's functions spherical-harmonic representation is truncated at $L_{\max}=3$, where $L\equiv(l,m)$. The von-Barth-Hedin[43] local spin-density approximation (LSDA) as parameterized by Moruzzi *et al.*[44] is used. We represent the site-dependent Voronoi polyhedra[45] (VP) in an atomic-sphere approximation (ASA).[46,47] Energy integrations of the Green's functions are done by complex-energy contourintegration[38] with 22 energy points on Gauss-Chebychev contour. The Brillioun-zone integration are based on the Monkhorst and Pack[48] special k-point method. For A1 cells, the number of k points was $20\times20\times20$. For defected cells with high-aspect ratio, 8 or 12 k points were used along the real-space long axis to ensure a good k-point distribution. The estimated error in relative energy differences within the given approximations is ±0.2 mRy (±32 K), relevant to the temperature predicted later.

For improved energies, we use an optimal KKR basis set determined from the saddle-point radii (SPR) found from topology of the charge densities at each site.[49] For any configuration, the SPR define the inscribed muffin-tin (MT) sphere for each site such that the density is well represented by spherical-harmonic expansion and there is almost constant interstitial density; in effect, the MT-SPR adjust to an atom's local "size." These MT-SPR permit the direct determination of volume-conserving, convex VP. However, here, we represent each VP within an ASA (radii determined from the MT values[49]) and include muffin-tin corrections[50] to account for the effect of interstitial electrons. The KKR-SPR-ASA provides formation enthalpies ΔE_f similar to full-potential methods, and resolves previous issues with the CPA associated with the representation of charge.[49] Besides improved energetics, charge-transfer effects are more physical and follow expectations from electronegativity,[49] and give similar results to the Bader cells.[51] Domain walls will not alter the type of defects because MAE are μRy while defect energies are mRy.

To verify our results, we calculated the FM defect energies using the Vienna *ab initio* simulation package (VASP) (Ref. 52) that uses pseudopotential and a projector augmented wave (PAW) basis,[53] with a 350–400 eV plane-wave energy cutoff, and find agreement between KKR-SPR-ASA and VASP results. VASP is computationally demanding for defect cells, and it does not address magnetic and chemical disorder, as is possible with KKR-SPR-CPA. We used the same exchange correlation and k meshes as in the KKR calculations, and include some generalized gradient approximation (GGA) results. Convergence of the VASP total energies (forces) is less than 2 meV/atom (30 meV/Å).

For completeness, we note that the competing magnetic states in bcc and fcc iron[54,55] and their relative stability using GGA versus LSDA has been well studied.[56,57] Within spherical approximations, A2 Fe is the ground state with LSDA because A1 is affected more than A2 by spherically averaging the potential,[54,57,58] as well as the approximations to the interstitial Coulomb energy.[58] Using the full potential linearized augmented plane-wave (FLAPW), Singh *et al.*[57] showed that GGA stabilizes A2 Fe versus A1 Fe in contrast to full-potential LSDA results,[54] with similar findings for FM versus antiferromagnetic (AFM) states; concomitantly, they also found improved structural properties. Bagno *et al.*[56] had already shown similar results using linear muffin-tin orbital (LMTO)-ASA with combined corrections, which ameliorate errors related to the spherical and interstitial approximations. For example, VASP-LDA predicts $L1_0$-FePd to be unstable, while in agreement with experiment VASP-GGA and KKR-SPR find it stable. Thus, we expect some differences in our ΔE_f compared to experiment due to LSDA errors in calculating the total energy of magnetic Fe.[54,58] However, at fixed composition, we expect (and find) accurate energy differences and defect energies because this systematic error is canceled.

In the remainder of this section, we define the relevant thermodynamic and energy assessments needed.

A. Formation enthalpies and defect energies

For stability and thermodynamics, we compare two types of energy difference: (i) the formation enthalpy or energy for each magnetic state and chemical phase,

$$\Delta E_f = E^{\text{alloy}}(V_0;\{R_\alpha\}) - \sum_{\alpha=1}^{S} c_\alpha E^\alpha(V_\alpha^0;R_\alpha^0), \tag{1}$$

the alloy energy relative to the concentration-weighted sum of the energies of the α constituents at their equilibrium volumes, and (ii) the planar-defect energy,

$$\gamma_{\text{def}} = \frac{E_{\text{def}}(N;\{R_\alpha\}) - E_0(N;\{R_\alpha\})}{m\text{A}_{\text{def}}} \tag{2}$$

with E_{def} the energy per m defects in an N-atom cell with a planar-defect area of A_{def} given relative to the undefected energy E_0. Care must be taken to keep the same stoichiometry in the defected and undefected supercells, see Appendix A. Importantly, defect energies are less dependent on the exchange-correlation and other approximations due to the inherent cancellations.

These energy differences depend on the MT-SPR or ASA radii $\{R_\alpha\}$ used in the basis. The set of radii $\{R_\alpha\}$ in ΔE_f differ for the alloy and elements. Because the defected and undefected cases have the same composition and unit cell, variational behavior is expected for $\gamma_{\rm def}$ in Eq. (2) but not for ΔE_f in Eq. (1). That is, one must know *a priori* the set of $\{R_\alpha\}$ that will produce an optimal ΔE_f because it cannot be chosen by direct variation.[49] We provide an example of these features below.

Schematics of perfect and defected $L1_0$ (compared to A1) are shown in Table I. The other figures show the CDBs, APBs, and twins that we address, along with the number of layers of atoms separating the defects and the defect area. The number of layers in the supercell is chosen to be the smallest value such that the defects are noninteracting. Each cell is defined with two translation vectors parallel, and the third normal, or nearly normal, to the defect plane (so m may be 1 or 2), centered on an inversion center to preclude any symmetry-induced dipole moments (needed for an ASA without multipoles), as described in Appendix A.

While it is certain that CDBs lie in the {011} planes, the APBs may lie in any crystallographic plane, as exemplified in Table I. For clarity, we designate the (001) direction to coincide with the tetragonal c axis. For APBs, there are two cases: (1) the defect planes can occur between atomic planes or (2) at an atomic plane requiring 50% disorder on all sites in that plane. For simplicity, we only address case (1). In addition, we have calculated the (111) twin energies, which are low energy by symmetry.[59]

B. Verification of optimal SPR basis

In Sec. II A, we discussed that defect energies exhibit a variational minimum, unlike ΔE_f.[49] In Fig. 2 for FePd, we show how $\gamma_{\rm CDB}^{011}$ and ΔE_f, obtained by variation in $R_{\rm Pd}^{\rm ASA}/R_{\rm Fe}^{\rm ASA}$, compare with those calculated at the set of saddle-point radii defining the MT-SPR basis. We find that $\gamma_{\rm CDB}^{011}$ is 106 $\rm mJ/m^2$ versus 101 $\rm mJ/m^2$ using MT-SPR. Both results agree well with the 110 $\rm mJ/m^2$ from VASP-PAW. The lower panel shows ΔE_f of $L1_0$-FM FePd versus $R_{\rm Pd}/R_{\rm Fe}$. We take the "correct" ΔE_f at the optimal SPR,[49] which then agrees with full-potential results. The optimal value of $R_{\rm Pd}/R_{\rm Fe}$ in FePd is 1.052, in contrast to 1.042 and 1.133 for CoPt and FePt, respectively, for the same defect. Clearly, these ratios indicate the effective size of each atom for the topology of the charge density in each alloy configuration; that is, in $L1_0$ a Pt atom is ~4% larger than the Co in CoPt and ~13% larger than the Fe in FePt. In effect, the optimal MT-SPR reflects an atom's local size in a given structure, see Appendix B.

C. Energy of partial long-range order states

Along with A1 and PM states, the KKR-CPA can address partially ordered $L1_0$ states.[60] The LRO parameter η, with $0 \le \eta(T) \le 1$, has a finite jump of $\eta(T_c^-) \ge 0.7$ for a first-order (order-disorder) transition[61] but often $\eta(T_c^-) \ge 0.9$. The state of $L1_0$ order can be represented by a finite-amplitude, static *concentration wave*[60–63] with wave vector $\vec{k}_0 = \{001\}$. In terms of $\eta_{\{001\}}$, the site-occupation probability (concentration) for the Co or Fe with c axis along [001] is

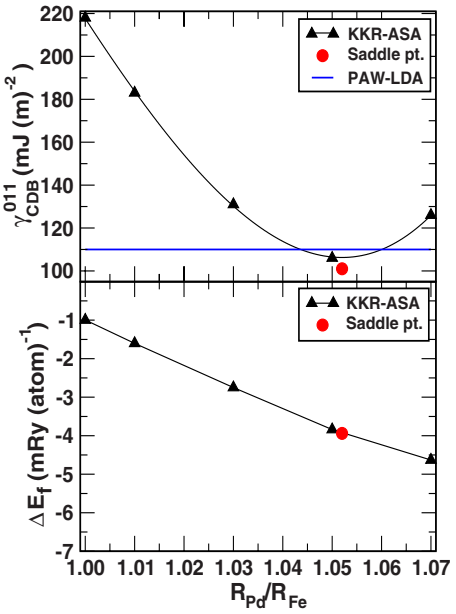

FIG. 2. (Color online) $L1_0$ FePd $\gamma_{\rm CDB}^{011}$ (upper in $\rm mJ/m^2$) and ΔE_f (lower in mRy/atom) vs $R_{\rm Pd}^{\rm ASA}/R_{\rm Fe}^{\rm ASA}$. KKR-ASA direct variation (triangles) and SPR basis (circle) at $R_{\rm Pd}^{\rm ASA}/R_{\rm Fe}^{\rm ASA}$ of 1.052, compared to VASP (horizontal line). $\gamma_{\rm CDB}^{011}$ from KKR-SPR-ASA is 101 vs 110 $\rm mJ/m^2$ from VASP.

$$c_i = \frac{1}{2}[1 + \eta(T)e^{i2\pi x_3}] = \begin{cases} \frac{1}{2}[1+\eta], & x_3 = 0 \\ \frac{1}{2}[1-\eta], & x_3 = \frac{1}{2} \end{cases} \quad (3)$$

showing two inequivalent sublattices. The value of $\eta(T)$ is obtained from thermodynamics, giving $\Delta c_i \propto \eta$ upon ordering. Recently, for example, $\eta(T)$ for $L1_0$-FePt was calculated via Monte Carlo simulations using effective pair-interactions-only obtained via a cluster expansion fit to VASP data,[64] and, similarly, tight-binding based on first-principles data.[36] Nonetheless, we can calculate energies for a fixed η, i.e., fully ordered (η=1), partially ordered ($0 < \eta < 1$), and disordered (η=0) state. Equation (3) dictates the sublattice c_i and we study the effect of thermally induced antisite defects on the $T_{\rm o\text{-}d}$. Alloys with higher $T_{\rm o\text{-}d}$ can have smaller $\eta(T_c^-)$ due to disorder stabilized by entropy.

Atomic pair correlations (or short-range order, SRO) are defined as $q_{\mu\nu,ij} = \langle(\zeta_i^\mu - c_i^\mu)(\zeta_j^\nu - c_j^\nu)\rangle$, where the site occupations $\zeta_i^\mu = 1$ (0) if the site i is (is not) occupied by a μ-type atom, and $\langle\cdots\rangle$ is a thermal average, and are associated with fluctuations δc_i. Thus, the free-energy change to second order in δc_i for homogeneous randomness is $\Delta F_{ord} = \frac{1}{2}\int d\vec{k} q^{-1}(\vec{k}) |\delta c(\vec{k})|^2$, when lattice Fourier transformed in the A1 state.[60] For a dominant SRO wave vector k_o, $\Delta F_{ord} \sim q^{-1}(\vec{k}_o) |\delta c(\vec{k}_o)|^2 \sim \eta^2$. Thus, energy and entropy changes are quadratic in η (Refs. 60) so $\Delta F_{ord}(\eta) \sim \Delta E_{ord}(\eta) \propto \eta^2$.

Such behavior explains the observed lattice anamolies in bcc-based Fe-Al,[42] where energy (not entropy) is the critical factor.

The KKR-CPA gives agreement for finite- and infinitesimal-amplitude cases, and resolved the mistaken comparison of $T=0$ K DFT and $T\neq 0$ K diffuse scattering results.[60] Notably, for second-order transitions, the SRO and LRO energy scales linearly with η^2; as such, the energy differences between fully disordered and ordered states should represent well the difference at the transition. When the chemical ordering energy $\Delta E_{ord}(\eta)$ deviates from being linear in η^2, then multibody interactions are at play,[60] which was later confirmed using cluster expansions.[65]

D. First- and second-order transitions

Here we establish approximate relations between $\Delta E_f(\eta)$ differences and first- and second-order transition temperatures. For first-order (order-disorder) transitions, the entropy is discontinuous, giving rise to a latent heat whereas in a second-order (PM-FM) transition, there is no latent heat and the entropy is continuous.

First-order. At $T_{\text{o-d}}$, the change in the Gibbs free energy $\Delta G(T_{\text{o-d}})=\Delta H(T_{\text{o-d}})-T\Delta S(T_{\text{o-d}})=0$, where ΔH and ΔS are jumps in enthalpy and entropy, respectively, between the two coexisting phases at $T^{\pm}_{\text{o-d}}$. Therefore,

$$T_{\text{o-d}}(c)=\frac{\Delta H(T_{\text{o-d}},c)}{\Delta S(T_{\text{o-d}},c)}\approx\frac{\Delta H_{\text{o-d}}(c)}{\Delta S_{\text{o-d}}(c)}\equiv T^{\text{MF}}_{\text{o-d}}(c). \tag{4}$$

The first equality is exact but difficult to evaluate. Thus, a mean-field solution is often assumed using the energies of the fully disordered ($T=\infty$) and ordered ($T=0$) states, i.e., $\Delta H_{\text{o-d}}\equiv H(\eta=0)-H(\eta=1)$, and similarly for entropy. Entropy of a fully ordered or phase-segregated state is taken as zero while that of the fully disordered binary is taken as the point entropy, i.e., $\Delta S_{\text{o-d}}(c)=-k_B\Sigma_\alpha c_\alpha \ln c_\alpha$. Generally, one must account for entropy due to SRO (LRO) in the disordered (ordered) phase.

Remarkably, for phase-segregating alloys with competing pair and multibody interactions, Zarkevich *et al.*[66] has shown, via Monte Carlo thermodynamic integration within a cluster expansion Hamiltonian, that the mean-field approximations give rather accurate estimates of the miscibility gap temperature $T_{\text{misc}}(c)$. This was not true for $T_{\text{o-d}}(c)$, however. For a pair-dominant cluster expansion found in numerous systems, the $T_{\text{o-d}}$ is empirically observed to be given accurately (within 4%) by[66,67]

$$k_BT^{\text{MF}}_{\text{o-d}}(\eta)=E^{\text{A1}}_{\text{PM}}(0)-E^{\text{L1}_0}_{\text{PM}}(\eta)\approx\eta^2\Delta H_{\text{o-d}}. \tag{5}$$

(The PM state indicated here is reflecting our enthalpies in Sec. III.) The latter approximation holds only if $E^{\text{A1}}_{\text{PM}}-E^{\text{L1}_0}_{\text{PM}}(\eta)$ is linear in η^2, as found for pairwise-dominant Hamiltonians. In which case, Eq. (5) is evaluated at $\eta=1$ rather than $\eta(T^-_{\text{o-d}})$. Notably, the Bethe approximation for a cluster expansion with arbitrary-ranged pair interactions has an identical form.[66] For states that are off-stoichiometric or quenched, Eq. (5) must use $\eta\neq 1$.

Second-order. As noted in Sec. II C, the energy and point entropy from SRO (small η) contribute only to second order in η. Hence, for FM transitions we expect

$$k_BT^{\text{MF}}_c\approx E^{\text{L1}_0}_{\text{PM}}(\eta)-E^{\text{L1}_0}_{\text{FM}}(\eta) \tag{6}$$

to be quite accurate. ($L1_0$ PM and FM states are specified from the results in Sec. III.) Although $\eta\neq 1$ generally, we use $\eta=1$ because we are comparing the same ordered state in the PM versus FM state.

TABLE II. KKR-ASA ($T=0$ K) and room-temperature (RT) measured a (in Å) and c/a (in parentheses) for A1 and $L1_0$ alloys in comparison to other theory results.

	CoPt	FePd	FePt
A1-PM			
KKR-ASA	3.780	3.760	3.750
Expt.[a]	3.810[b][3.77]	3.815[b]	3.800[b]
Other LDA[c]	3.750		3.750
$L1_0$-FM			
KKR-ASA	3.784 (0.984)	3.78 (0.966)	3.810 (0.970)
Expt.[d]	3.800 (0.972)[b]	3.85 (0.966)[b]	3.860 (0.966)[b]
Other LDA[e]	3.746 (0.967)	3.81 (0.975)	3.772 (0.975)
Other GGA[f]	3.819 (0.973)	3.82 (0.961)	3.872 (0.973)

[a]Reference 68 for CoPt: PM phase at 1100 K has $a\sim 3.77$ when extrapolated to RT Ref. 69 for FePd and Ref. 70 for FePt.
[b]Not extrapolated to room temperature or 0 K.
[c]TB-LMTO: Ref. 71 for CoPt and Ref. 72 for FePt.
[d]Reference 6.
[e]VASP-LDA: CoPt (this work) and FePt (Ref. 73). FLAPW for FePd (Ref. 74).
[f]VASP-GGA: CoPt and FePd (this work). Reference 73 for FePt.

III. RESULTS AND DISCUSSION

For CoPt, FePd, and FePt, we present our results for the optimized structural parameters, formation enthalpies, and defect energies using KKR-CPA with an optimal basis determined from saddle points in the electronic density. We compare our results with known experimental data or results from more accurate (full-potential or PAW) methods. We present the accurate thermodynamic predictions of T_c and $T_{\text{o-d}}$ temperatures. We also correlate the energetics to the electronic density of states (DOS) for each alloy. Our ability to address more realistic annealing conditions and characterization behavior of these processed materials is important when comparing to measurements, or providing energetics for use in coarse-grained modeling.

A. Structural properties

In Table II, we show the optimized lattice parameters a (in Å) and c/a ratios for A1 and $L1_0$ alloys. For all the three systems, our calculated a differ from a_{exp} measurements[6,68–70] by $<2\%$, as expected for LSDA.[38] Our SPR-derived LDA results lie between results from LDA and GGA from more exact methods.[71–76] In addition, our results agree well with measurements extrapolated to low tempera-

TABLE III. KKR-CPA formation enthalpies, ΔE_f (in mRy/atom) for A1 and $L1_0$ in PM and FM states. Available experimental and theory results are provided for comparison.

System	Phase	ΔE_f	Expt.	Other
CoPt	A1-PM	+4.65		
	$L1_0$-PM	−2.60		
	A1-FM	−5.14	-9.5 ± 1.91 [a]	-7.5 ± 1.91 [b]
				−4.85 [c]
	$L1_0$-FM	−6.98	-10.3 ± 1.62 [a]	−5.81 [d]
				−6.55 [e]
				−8.38 [b]
FePd	A1-PM	+7.82		
	A1-FM	+1.08		
	$L1_0$-PM	+0.80		
	$L1_0$-FM	−3.94	-7.2 ± 0.8 [a]	+2.94 [d]
			−7.1 [a]	−9.56 [e]
				−10.6 [b]
FePt	A1-PM	−3.97		
	A1-FM	−13.17		−12.5 [f]
	$L1_0$-PM	−16.48		
	$L1_0$-FM	−21.13		−21.3 [b]
				−10.3 [d]
				−16.5 [g]
				−23.5 [f]

[a]Expt.: CoPt Ref. 77 and FePd Refs. 77 and 78.
[b]Thermal assessment: CoPt and FePd Ref. 75 and FePt Ref. 76.
[c]KKR-SPR for A1 using special quasirandom structures (Ref. 74).
[d]VASP-LDA (this work) or Ref. 73 for FePt.
[e]VASP-GGA for FePd and CoPt (this work).
[f]Reference 73 used analytic bond-order potential.
[g]VASP-GGA for FePt from Ref. 73.

tures, as in A1 CoPt where we obtain 3.78 Å compared to the observed (extrapolated) 3.77 (<0.2% error); and similar results are expected for extrapolated $L1_0$ results. We also note that c/a is important in determining the correct magnetic state.[34]

B. Formation enthalpies

In Table III, we provide ΔE_f for FM and PM A1 and $L1_0$ states for the three alloys, and compare to other experimental[77] and theoretical[49,73,75,76,78] results. The optimal basis KKR-SPR-ASA dramatically improves agreement with experiment or full-potential methods.[49] The ΔE_f is absolute measure in each system whereas all other energies relevant to $T_{o\text{-}d}$ or T_c are relative energies. The $L1_0$-FM-CoPt ΔE_f matches fairly well with that of VASP, and the empirical modeling of de Boer *et al.*[75] Also, ΔE_f for A1-FM-CoPt agrees with A1 approximated by special quasirandom structures,[49] as also shown in Table III. Even so, ΔE_f for A1 and $L1_0$ lie outside the large experimental errors. Our ΔE_f for $L1_0$-FM-FePt also compares well with other theoretical data.[73,76] In FePd, there is large span of theoretical values depending on DFT method and functional, see Sec. II.

For all three alloys, the order of the equilibrium transformations with increasing temperature observed in each phase diagram[79–82] is $L1_0$-FM to $L1_0$-PM (a Curie transition) and then $L1_0$-PM to A1-PM (an order-disorder transition). Considering only energy differences in Table III, the sequence is not obviously reproduced, as the entropy jumps are ignored that favor certain transitions. For CoPt, for example, our ΔE_f given in Table III reproduces the equilibrium observed order, except that the A1-FM phase lies in between the FM and PM $L1_0$ phase whereas, for FePt, the ΔE_f appears to mirror the observed phase changes because the A1-FM lies above $L1_0$-PM and entropy favors the $L1_0$-PM to A1-PM to occur, as observed. However, if samples are annealed in a magnetic field, A1-FM phases are found. Using differential scanning calorimetry, Barmak *et al.*[83] measured the A1-FM to $L1_0$-FM transformation enthalpies in CoPt and FePt thin films to be 2.36 ± 0.15 mRy and 7.77 ± 1.60 mRy, respectively, and these compare reasonably well to our 1.84 mRy and 7.96 mRy in Table III so the calculated order appears to be correct.

Our FePd results almost mirror those of FePt, except the energy differences are much smaller; for example, A1-FM is only slightly (0.28 mRy or 44 K) higher than the $L1_0$-PM, which is degenerate within our error. However, for Fe-based alloys we acknowledge the issue of LDA versus GGA stability, see Sec. II, especially for A1-FM relative to A1-PM but which is not relevant to the $T_{o\text{-}d}$ or T_c determined here.

Comparing our results with other measured values and DFT results confirm that our energy differences are accurate. For example, MacLaren *et al.*[84] used VASP to estimate the A1 ΔE_f from an eight-atom unit cell containing four $L1_0$ cells. Considering symmetry, there are at least four distinct configurations with which to approximate an ensemble average,[84] giving an energy difference between FM A1 and $L1_0$ FePt of 8.3 mRy (or 1311 K), agreeing well with our KKR-SPR-CPA value of 8 mRy (or 1264 K). However, these FM energy differences are not relevant to $T_{o\text{-}d}$ (as used in Ref. 84), which occurs in the PM phase.

C. Transition temperatures

We use the estimates for transition temperatures given in Sec. II D, without resorting to more sophisticated modeling, see Refs. 65 and 66, and references therein. Table IV compares our T_c and $T_{o\text{-}d}$ estimates from solely KKR-SPR-CPA energy differences to the observed values,[6,85,86] where our T_c is within 4% of experiment. We expected our T_c to be a good estimate because we compare the same ordered phase with and without localized magnetic disorder (related to local exchange splitting) whereas $T_{o\text{-}d}$ involves ensemble-averaging effects. Any disorder will reduce our energy differences; so, our calculated $T_{o\text{-}d}$ should be higher than experiment until the effect of the observed partial order is taken into account, see Table IV.

Except for FePt (24% higher than observed), the calculated $T_{o\text{-}d}$ is within 4% of that observed, see Table IV, suggesting that our energies differences and mean-field estimates are quite accurate. The discrepancy for FePt arises, as we show below, due to the missing effect of partial LRO

TABLE IV. KKR-ASA energy differences (in kelvin) between (a) FM and PM $L1_0$, and (b) PM A1 and $L1_0$. From Sec. II, we estimate our relative error as ±30 K. Observed T_c and $T_{o\text{-}d}$ are from Ref. 6, with (second line) Ref. 85 for FePd and Ref. 86 for FePt. We use $L1_0(\eta=1)$ except to address effects of finite-T antisite disorder, as noted in text.

Temperature (K)	CoPt	FePd	FePt
$(E_{PM}^{L1_0}-E_{FM}^{L1_0})/k_B$	692	749	735
T_c (expt.)	720	730	750
		723	745(735)
$(E_{PM}^{A1}-E_{PM}^{L1_0})/k_B$	1145	1109	1977
with $\eta=0.98$	1100	1065	1899
with $\eta=0.90$			1586
$T_{o\text{-}d}$ (expt.)	1100	1050	1600

(antisite disorder) in $L1_0$-PM because the transition occurs at 60% higher temperature than for CoPt and FePd. Indeed, measurements in FePt find $0.8 \leq \eta \leq 0.95$ depending on annealing time and sample preparation. Depending on the milling time of the powdered sample, a similar effect (although less sensitive) was also observed by Lyubina *et al.*[86] for the Curie temperature. The observed T_c of 745 (735) K for FePt in Table IV were found after milling for 4 (7) h,[86] remaining in agreement with our results.

D. Effects of thermal antisites on T_{od} and MAE

Diffraction experiments often have difficulty finding η accurately as they are measured relative to the low-T intensity where complete order is assumed, yet slow kinetics limits the correctness of this assumption. In FePt, η changes from 0.84 with 0.5 h of annealing at 773 K to near 1.0 for 250 h.[87] Notably, $\eta(T_{o\text{-}d}=1600\ \text{K})$ is 0.81 but increases toward (the assumed) 1.0 at 773 K. Kinetics of the transformation in nanocrystalline FePt have been studied,[86] and annealing sensitivity was also found, reporting that $\eta \approx 0.95$. Thin films of 50–60 nm thickness have $\eta \approx 0.93 \pm 0.05$.[88] Hence, η ranges from 0.81 to 0.95 in the cited experiments. Also, $\eta(T)$ was extracted from Monte Carlo simulations based on effective pair interactions[64] derived from DFT data, yielding a $T_c \sim 1500$ K and $\eta \sim 0.6$, smaller than observed.

To address the effects of partial order on the PM energetics and $T_{o\text{-}d}$, we calculated the $E^{A1}-E^{L1_0}(\eta)$ versus η^2 in the PM state, see Fig. 3. As is evident, for the partial-ordered, Fe-based alloys, $\Delta E^{ord} \simeq \eta^2[E_{PM}^{A1}-E_{PM}^{L1_0}(1)]$, indicating ideal ordering behavior and dominant chemical pair interactions, see Sec. II C. In contrast, CoPt is somewhat nonlinear, indicating that multibody interactions are relevant.[60] Near complete order ($\eta \sim 1$), both FePd and CoPt exhibit similar values of $T_{o\text{-}d}$, as observed.

For FePt in Fig. 3, ordering is strong, i.e., the slope is large, making $E^{A1}-E^{L1_0}(\eta)$ more sensitive to partial LRO, especially compared to CoPt and FePd. As shown in Table IV, we calculate $T_{o\text{-}d}$ as 1977 K at $\eta=1$, significantly above the observed value of 1600 K, and outside our estimated

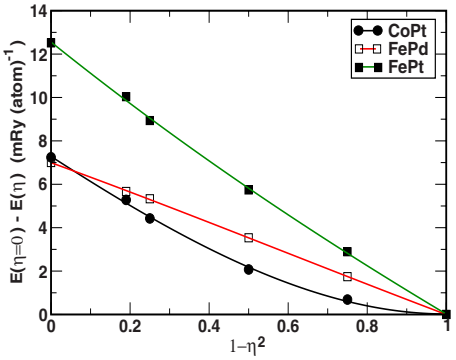

FIG. 3. (Color online) KKR-SPR-CPA $E^{A1}-E^{L1_0}(\eta)$ for CoPt-PM (circles), FePd-PM (open squares) and FePt-PM (squares), showing the effects of partial LRO on $T_{o\text{-}d}$.

error. Now, we placed 5% disorder on the two $L1_0$ sublattices, i.e., $\eta=0.9$ in Eq. (3), as suggested from experiment. The enthalpy difference between the A1-PM and $L1_0$-PM phase is 1586 K at $\eta=0.9$, a 21% reduction from the $\eta=1$ result. Therefore, a small, expected amount of antisite disorder fully explains our discrepancy when we (incorrectly) assumed perfect order at the transition, see Table IV. If Eq. (5) is used, i.e., $T_{o\text{-}d}(\eta)=\eta^2 1977$ K, then $T_{o\text{-}d}$ is 1601 K for $\eta=0.9$, compared to direct calculation of 1586 K, within our estimated relative error.

Similarly, for CoPt and FePd, thermal disorder is also expected but it must be much less than for FePt because the $T_{o\text{-}d}$ is 40% less than FePt. With a small 1% antisite disorder ($\eta=0.98$) for CoPt and FePd, the $T_{o\text{-}d}$ lowers slightly and improves relative to the measured values, see Table IV, remaining within our relative error.

The MAE is also strongly correlated to the LRO. MacLaren *et al.*[89] showed that the MAE, defined in a Néel model as $E^{MAE}=\frac{1}{2}\Sigma_{nn}K_U^{nn}\cos^2\theta_{nn}$ for interactions between near-neighbor magnetic moments, have $K_U(\eta)$ change with partial order[84] as $K_U(\eta) \sim \eta^2 K_U(1)$, for reasons stated in Sec. II C. Shima *et al.*[90] measured $K_U(1)$ of 2.1×10^7 ergs/cm^3 at 4.2 K for FePd, whereas it is 2.6×10^7 ergs/cm^3 at 300 K.[91] They also studied the concentration dependence of $K_U(\eta)$, which reduce to 1.6×10^7 ergs/cm^3 at 57% Pd. They reported an assessment of $\eta=0.9$ at 300 K for FePd,[90] which they assumed did not vary up to the $T_{o\text{-}d}$. Also, Hirotsu *et al.* (see Ref. 89) suggested that the measured $\eta=0.65$ via x-ray diffraction explained why their $K_U(1)$ of 2.6×10^7 ergs/cm^3 for $L1_0$-FePd agreed with the 1.0×10^7 ergs/cm^3 for their off-stoichiometic sample.

From Sec. II C for an A-B off-stoichiometry alloy c_B near $c_B^{L1_0}$, the maximum LRO parameter is

$$\eta^{\max} \leq \begin{cases} c_B/c_B^{L1_0} & \text{for B-poor alloys} \\ (1-c_B)/(1-c_B^{L1_0}) & \text{for B-rich alloys.} \end{cases} \quad (7)$$

Hence, assuming perfect order for $L1_0$ Fe-50%Pd, at best, $K_U\eta^{\max}=(0.43/0.50)^2K_U$ [Eq. (1)] or 1.55×10^7 ergs/cm^3 for $L1_0$ Fe-57%Pd, which is the observed value. (A similar result is found for Hirotsu data.) Because c/a varies roughly linearly with c_{Pd}, or equivalently η^{max}, there must be a similar correlation of K with $(c/a)^2$, as is indeed observed.[90]

E. Finite-size effects: Nanoparticles

The superparamagnetic behavior (magnetization direction reversal induced by thermal fluctuations) of NPs is the main physical limitation for magnetic-storage technology. The thermal stability of the magnetization can be assessed by the quantity[92] $\beta K_U V > 60$, where V is the volume of the magnetic domain. However, the stability of the ordered phase giving rise to the magnetoanisotropy is also relevant, for, if the phase becomes unstable at smaller dimensions, then the advantage of the alloy NPs is also lost. Here we assess from finite-size scaling theory the $L1_0$-FePt Curie temperature versus size using only the bulk energetics that we have calculated. We show that the dramatic decrease in ordering temperature of $L1_0$ coincides with the observed size for the superparamagnetic limit and the loss of $L1_0$ stability in the NP given by relative DFT ΔE_f of various NP configurations.

For simplicity, for a particle composed of n_{cells} fcc cubes on a side, we can define an approximate diameter of a NP by the geometric mean of the side and diagonal of a cube n_{cells} fcc cells on a side, i.e., $d=3^{1/4}an_{\text{cells}}$. For FePt or CoPt, $d \sim 3$ nm is where stability of $L1_0$ is lost to other morphologies,[4,32] which is about n_{cells} of 6, or ~864 atoms. A similar size is required in bulk Ni to sustain a local moment.[93] Using nanobeam electron diffraction, it is observed[94] that $L1_0$ FePd NP larger than 8 nm have a mean LRO parameter η of 0.79, reducing rapidly in smaller particles, where the reduction in hard magnetic properties, including MAE,[95] is attributed to this reduction.[96] Small NPs exhibit superparamagnetic behavior due to thermally induced magnetic disorder, below 6 nm in FePd, and loss of $L1_0$ stability.[94,96] Similar behavior occurs in NP films.[37] Monte Carlo simulations for $L1_0$ FePt truncated-octahedron NPs, which include the effects of surface segregation, find similar results, with estimated 4.4 nm size for the superparamagnetic limit.[36]

If finite-size effects dominate, then, according to finite-size scaling,[97,98] T_c will scale with T_c^{bulk} in Eq. (6) as

$$T_c(d) = T_c^{\text{bulk}}[\eta(T)]\left(1 - \left[\frac{d}{d_0}\right]\right)^{-1/\nu} \tag{8}$$

with $\nu \approx 2/3$. Equations (6) and (8) also depends on $\eta(d)$, which decreases with NP size. In Fig. 4, we show the results of Eq. (8) for possible d_0's, an effective size where magnetic stability is lost, and it reproduces the observed trends in FePt (Refs. 16, 37, and 86) and FePd,[94] for d_0 between 2 and 3 nm, which is consistent with most experimental results.

However, experimental results depend critically on whether the particles are free-standing, stabilized with ligands, in a solvent or matrix, or processed in thin-film form. For FePt particles in solvent and salt matrix, Rong *et al.*[16] found from fitting their data to Eq. (7) that $d_0 \sim 0.9$ nm, and their best fits gave an effective T_c^{bulk} much larger than the true value. They also measured the effect of size on the LRO, finding that the NP are fully ordered for $\eta(d > 14$ nm), which is not even true in bulk alloys nor in other measurements on NPs.[4,94–96] The discrepancy may be due to solvent effects or to errors in relative intensity measurements used to estimate η. In CoPt NPs, it has been found that shape and smallest caliper dimension highly affects $T_{\text{o-d}}$, so morphology is critical.[4] Using $\eta(d)$ in Eq. (5) will result a similarly observed decrease in $T_{\text{o-d}}$, although this ignores morphological changes.

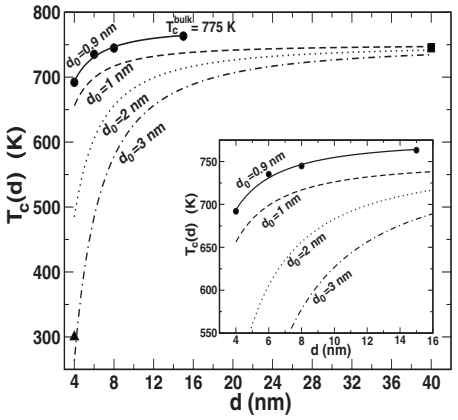

FIG. 4. Scaling results for T_c vs NP diameter d for various d_0 in Eq. (8). FePt data is from Ref. 16 (circles), Ref. 37 (triangle), and Ref. 86 (squares). Reference 16 data is for NPs in solvent/salt matrix so it is shown by fitted value of effective bulk, see text.

F. Electronic density of states

In Fig. 5, we provide the atom-projected (broken lines) and total (solid lines) electronic DOSs for the $L1_0$-FM (left panel) and $L1_0$-PM (right panel) phase of CoPt, FePd, and FePt alloys, respectively. These DOS are plotted with respect to the electronic chemical potential or Fermi level E_F, with the electron majority-(minority-) spin manifold shown above (below) the DOS zero line.

For all three FM alloys, there is a similarity between majority DOS and its occupation but the minority DOS occupancy is predominantly given by moving E_F rigidly from Fe to Co in Pt-based alloy. Although the majority DOS for FePd is similar to the other alloys, its bandwidth is much narrower than those of the Pt-based alloy; this destabilizes FePd relative to FePt. Primarily, these differences between FePt and FePd arise from relativistic (Darwin and mass-velocity) effects that pull the s states lower in energy for FePt, permitting the filling of lower-lying, hybrid-t_{2g} states formed between Fe and Pt, similar to NiPt, which gives rise to known size effects.[99]

In contrast, the PM DOS in the three alloys show that the magnetization-projected (↑ and ↓) electronic DOS for Co and Fe are very different, with significant states of antibonding character above E_F. This general feature is observed in systems with large local magnetic moments (i.e., exchange splitting), and originates from the extra scattering in the DLM state caused by the difference in the atomic potentials due the orientational disorder of the magnetic moments. Considering only band-filling effects the PM DOS for $L1_0$ shows that CoPt should behave differently than FePd and FePt because Co has one additional electron that moves E_F further into the antibonding d states; however, CoPt and FePd ultimately show similar ordering energetics because FePd does not have

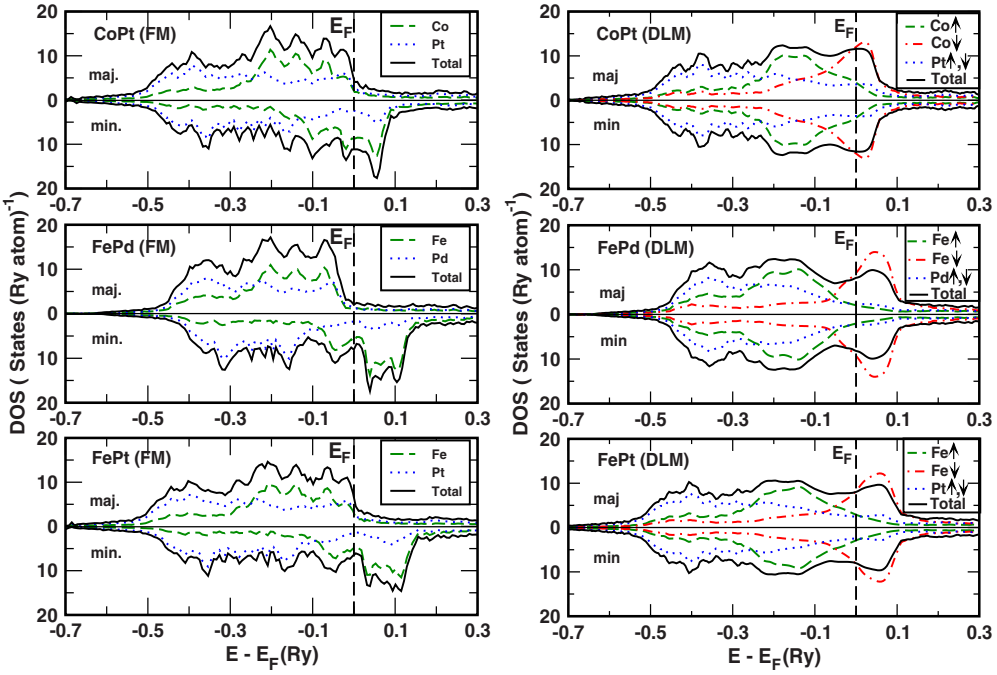

FIG. 5. (Color online) Atom-projected and total density of states for $L1_0$-FM (left panel) and $L1_0$-PM (right panel) CoPt, FePd, and FePt alloys calculated from the KKR-ASA method. In the left panel, dashed and dotted lines indicate the atom projected DOS and the solid line the total DOS. In the right panel, dashed (green) and dotted-dashed (red) lines indicate the Co (or Fe) spin-up and spin-down projected DOS, the dotted (blue) line indicates the Pt (or Pd) spin-up or spin-down projected DOS and the solid (black) line the total DOS. Fermi levels are indicated by the dashed vertical line.

the same increase in stability from the relativistic shift of *s* states as found in CoPt.

In terms of band energy, the FM state is always less favorable than the PM state. By transforming from PM to the FM $L1_0$ state there is a favorable gain in potential energy; in fact, the change in Madelung energy from increased charge transfer in the FM state relative to the PM state is almost entirely the origin of the energy differences appearing in Table III and IV. For example, in CoPt the FM state has $\pm 0.448e$ non-neutral charges on the Co and Pt sites, respectively, where Co (Pt) has deficient (excess) charges compared to the PM state with $\pm 0.438e$. The Madelung energy difference between the PM and FM $L1_0$ states then give a gain in stability of 4.3mRy versus 4.4mRy from total-energy difference, see Table III. A similar result holds for FePt and FePd.

In Table V, the local magnetic moments in each state are compared. For $L1_0$-FM, the moments of the 3*d* atoms are roughly 10% larger than in the A1-PM, except for FePd which is only 3% larger. Overall, we agree with previous calculations and with most experimental results. However, the measurements[101] on FePd were thin-film wedges grown on MgO and were sensitive to chemical order; oddly, they have Fe moments smaller than bulk Fe, and the Pd moments were significantly larger than any other reported. For FePt, the moments of Pt were not reported,[102] although the average moments were, suggesting that the moments may be arranged ferrimagnetically. We note, however, that anti-FM states are close in energy and sensitive to c/a,[34] and, as discussed, sample magnetization is sensitive to sample preparation, strain, and concomitant tetragonal distortions; therefore, we have some reservation for comparing to those measurements.

Unlike the FM state, Pd and Pt become nonmagnetic in the PM state from the collapse of local moment at their site in the DLM approximation; that is, they cannot maintain polarization because the average neighboring magnetic moment is zero. If magnetic SRO was included, these atoms

TABLE V. For A1 and $L1_0$, the KKR-ASA local magnetic moments (in μ_B) and average moment (in parentheses), with comparison to observed and other calculations. DLM Pd and Pt moments are zero so only three-dimensional moments are provided.

	CoPt	FePd	FePt
A1-PM			
KKR-ASA	1.46	2.78	2.46
$L1_0$-PM			
KKR-ASA	1.41	2.83	2.63
$L1_0$-FM			
KKR-ASA	1.73, 0.39	2.85, 0.38	2.84, 0.34
	(1.01)	(1.62)	(1.60)
Expt.[a]	1.76, 0.35	2.04, 0.62	2.80,
	(1.05)	(1.33)	(0.77)
Other LDA[b,c]	1.74, 0.35	2.90, 0.35	2.82, 0.33
	(1.04)	(1.62)	(1.58)
Other GGA[b]	1.83, 0.37	3.02, 0.34	2.96, 0.34
	(1.10)	(1.68)	(1.65)

[a]Reference 100 for CoPt: Ref. 101 for FePd: Ref. 102 for FePt
[b]FP-LMTO: Ref. 103 for CoPt, FePd, and FePt.
[c]ASW: Ref. 104 finds 1.60 (0.30)μ_B for Co (Pt). Reference 105 finds 2.92 (0.37)μ_B for Fe (Pt).

TABLE VI. Planar-defect energies (γ in mJ/m^2) for FM and PM $L1_0$ cases. The upper (lower) values are FM (PM). In bulk alloys (111) twins must occur in pairs, although they do form singly in NPs. (110) and (001) APBs occur in pairs (see Table I), with one defect having neighboring planes of pure Co(Fe) and the other defect having Pt(Pd). Intrinsic stacking faults and twins do not occur on the parent lattice as with ordering defects, see Table I.

γ_{def}	CoPt		FePd		FePt	
	KKR	VASP	KKR	VASP	KKR	VASP
$\gamma_{\text{CDB}}^{011}$	148	147	101	110	323	365
	193		94		404	
$\gamma_{\text{APB}}^{010}$	48	60	136	170	286	249
	57		91		305	
$\gamma_{\text{APB}}^{111}$	169	139	197	235	265	229
	234		152		311	
$\gamma_{\text{APB-pair}}^{110}$	287	321	294	312	368	327
	321		269		390	
$\gamma_{\text{APB}}^{011}$	265	298	264	293	319	367
	290		198		495	
$\gamma_{\text{APB-pair}}^{001}$	1003	863	982	887	865	765
	1147		1076		971	
$2\gamma_{\text{twin}}^{111}$	94	111	161	191	281	253
	102		123		302	
$\gamma_{\text{ISF-1}}^{111}$	352	402	392	432	672	631
	431		351		787	
$\gamma_{\text{ISF-2}}^{111}$	515	475	452	495	689	644
	717		402			

could have a small induced moment. Note that Pt and Pd atoms, although near a magnetic instability in elemental state, acquire magnetic moments in the FM alloys due to the presence of magnetic neighbors Co and Fe with nonzero magnetization.

G. FM and PM planar defects energies

Having established that we can reproduce observed thermodynamic temperature scales, we can address the effect of processing samples in the PM versus FM states. For planar-defect energies in $L1_0$ CoPt-type alloys there are two key questions: *Which defects are likely to form and remain during processing and which of these are likely to pin magnetic domain walls?* The answer to the first question is dependent on geometry, strain energy, thermal processing, and defect energies (see Sec. I). The sensitivity of these results to partial LRO, which we can calculate directly, is important, especially when comparing to experimental data; generally, the defect energies decrease linearly with η^2 because in the A1 phase there are no ordering defects. Answering the second question requires MAE calculations, which we do not present here; these have been calculated for FM CoPt by Belashchenko *et al.*[106] Because annealing in each alloy takes place at temperatures above T_c, the PM defect energies are the pertinent ones for considering likelihood of their remaining in a sample during annealing.

Table VI shows the defect energies for the FM and PM states. For verification, our FM KKR-SPR-ASA results are within 10–20 % of the FM VASP results. For bulk samples (111) twins are formed in pairs, so we report them as $2\gamma_{\text{twin}}^{111}$. The (111) twins are low-energy defects by symmetry, and their calculated low energies correlate well with their being observed in the bulk alloys, e.g., FePt (Ref. 87) and FePd (Ref. 107) alloys. As discussed above, (011) polytwins relieve strain[6,13,17] and, hence, lower system energy in ways that cannot be addressed with small unit cells, except that the (011) CDB cell has relieved the strain between the two variants considered. In each alloy, the (001) APBs are highest in energy, which is likewise not surprising, as this requires planes of like atoms to be adjacent to one another, contrary to the tetragonal ordering (see figure in Table I). Stacking-fault energies are high but are significantly less than (001) APBs. Notably, stacking faults (SF-1) with the different atomic occupations in the same (001) plane but across the (111) defect (see figure in Table I) are 30% lower than those (SF-2) with the same atomic occupations across the defect plane, which is similar to configuration next to (001) APBs plane.

Beyond these observations, the alloys begin to show their separate characters. In CoPt and FePt, the PM defect energies are always higher than the FM ones; where in FePd they are mostly lower by 25–33 %, showing that processing in the PM state can alter the observed defects. Relative to the others, the PM (010) APB energy in FePd is the lowest along with the (011) CDB, which indicates that these are most

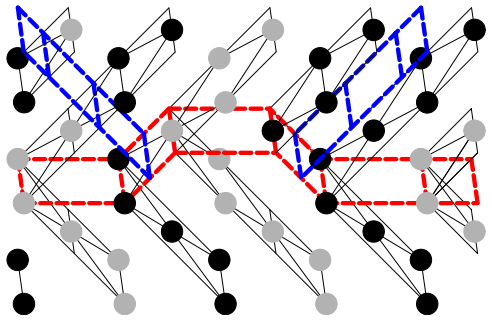

FIG. 6. (Color online) Termination of two APB variants dark-dashed (blue) lines, (010) and (001), at a CDB light-dashed (red) lines. This geometric ability of CDBs to terminate APBs may facilitate annealing out APBs.

likely to persist after prolonged annealing. Furthermore, the relatively similar values of APBs of varying orientations would allow the curved defect surfaces observed experimentally, see Sec. I, with some faceting due to preference for lower energy orientations, such as (010), and avoidance of higher energy orientations. In CoPt, we find (010)APB to be the most stable so we would expect APBs to align along this orientation and persist after the other orientations are annealed out. APBs with this orientation should be a strong candidate in studies of MAE in CoPt. FePt has the highest defect energies but also the highest $T_{o\text{-}d}$. Similar to FePd, when APBs are present in FePt, we should expect them have curved defect surfaces, again avoiding (001) orientations. Also, the defect energies in FePd are generally closer, which seems to be reflected in the micrograph Fig. 1(b), where APBs of multiple orientation are clearly present.

Which planar defects have a low probability of serving as domain-wall pinning centers because they are most likely to be annealed out during thermal processing? While some descriptions of domain-wall motion seem to exclude APBs (see Ref. 6, and references therein), it is possible that, due to processing, APBs were either not present or at low densities in these samples. APBs should occur during formation of the ordered phase but may be largely annealed out, particularly if their energies are high and/or during prolonged annealing. As we illustrate in Fig. 6, APBs can be terminated on CDBs, providing a mechanism to assist this process. The formation of *c* domains is driven by lowering the strain energy during ordering but once the strain energy has been relieved, the CDBs can also begin to anneal out. Such decrease in both APB and CDB density has been observed experimentally in bulk samples.[25] In all three alloys, though, we expect defects that assist in lowering the strain to persist. (111) twins are not ordering defects. However, they are also observed, both in bulk samples that have experienced prolonged annealing and in NPs, where (011) CDBs and APBs have not been observed.[3,108]

Thus, the question of which defects are present and/or serve as domain-wall pinning sites may depend on the particular alloy and its processing history, as suggested from our results. In all these alloys, the (001) APBs have the highest defect energy and should always anneal out most quickly. In both CoPt and FePd, the (010) APB is the most favored APB variant, and may compete to some degree with (011) CDBs, though the CDBs should persist due to strain energy; all the other APB variants should eventually anneal out. FePt, on the other hand, favors two APB variants, (111) and (010). Thus, if APBs do pin domain walls, these results coincide with observations that longer annealing times can decrease the coercivity of the materials, though the lowest energy defects are likely to persist. The relatively lower energies of the (111) twins in these materials may explain the appearance of (111) twins rather than (011) CDB in NPs and the increase in (111) twin density while (011) CDB decrease in density during prolonged annealing in bulk samples. Finally, for completeness we note that Zhang and Soffa,[13] by analogy to the behavior of domain-wall pinning via APBs in the Heusler ($L2_1$) FM Cu_2MnAl,[109] suggested that APBs pin domain walls in FePd. However, in the $L1_2$ FM Heusler alloy AFM atomic-layers form around the APB defects but FePd and CoPt do not appear to exhibit AFM behavior. $FePt_3$ does so Pt-rich defects [such as those occurring in the (001) or (110) APB pairs] may. We are searching for AFM alignment at defect boundaries but have none to report. It is important to mention at this point that stacking faults have been observed in A1 CoPt nanoparticles.[3] While stacking faults are typically formed in bulk samples via dislocation motion, in nanoparticles their presence has been attributed to coalescence. The two stacking-fault types in $L1_0$ depend on the relative shift of planes across the (111) defect plane, and, in principle, one type is equivalent to the other plus an antiphase boundary. While the $L1_0$ defect energies are high, it is possible that their formation is limited to the A1 phase.

We can conclude defect energies are different for the FM and PM phases. Specific APB orientations are favored but their exact relationship to macrodomain walls is unclear. The PM phase makes fewer defects favorable in CoPt (as observed) and more APBs more favorable in FePd (as observed). Although room temperature, FM behavior is of greatest interest, MAE calculations should consider those defects with the lowest defect energies under formation conditions, which are PM not FM. While both the experimentally observed macrodomain walls and the calculated APB energies favor specific orientations, the shapes of the observed APBs and the APB termination at CDBs due to geometry (see Fig. 6) are not consistent with the observed zigzag shapes of the macrodomain walls. The degree to which APBs pin magnetic domain walls in CoPt-type alloys would have to be quite weak, as it appears that domain walls do not follow the APBs directly as, for example, in the Heusler alloy.[109]

IV. SUMMARY

Because of their technological potential for ultrahigh-density magnetic-storage media and nanometer-sized grains, we have determined the formation enthalpies and defect energies for CoPt, FePd, and FePt alloys in A1 and $L1_0$ structures in both PM and FM states relevant to the processing of these materials, at temperatures where the structural transformations initiate. As planar defects form during processing, a subset is believed to act as pinning centers of magnetic domain walls within the ordered grains, impacting storage

properties. Using density-functional theory methods, we addressed the chemical and magnetic disorder and defect structures relevant to realistic processing conditions, including a connection to the underlying electronic structure. We quantitatively reproduced the observed order-disorder and Curie temperatures, which establishes relevant energy scales for defect formation and stability for better characterization of processed materials or for providing energetics for use in coarse-grained magnetic-domain modeling. We established that processing in different magnetic states alters the $L1_0$ defect energies and changes stable defects to those observed. We have also shown quantitatively that the properties of these alloys, while similar in some cases, do have variation that do not permit one to act as a prototype for the others. Finally, we made a connection between bulk and nanophase behavior, where scaling of properties agrees with the trends observed when attempting to increase bit density by decreasing NP size. For NPs below ~1000 atoms (~3 nm for the three alloys, similar to the observed superparamagnetic limit), the Curie temperature and MAE is lost due to the loss of stability of the high-coercivity $L1_0$ structure versus other morphologies of particles.

ACKNOWLEDGMENTS

We are supported by the Department of Energy (Grant No. DEFG02-03ER46026) and Lawrence Livermore National Laboratory (Contract No. B573247). Ruoshi Sun performed some verification and test calculations for Summer REU project (National Science Foundation under Grant No. DMR-0705089).

APPENDIX A: OPTIMAL CELLS WITH PLANAR DEFECTS

All defects are simulated in cells employing periodic boundary conditions. To reduce the N^3 computational cost, we choose the fewest numbers of both inequivalent atoms and total atoms N per cell, with careful use of symmetry often reducing the number of inequivalent atoms to $N/4$. For all defect calculations presented here two of the cell translation vectors were chosen to lie in the defect plane; the symmetries of $L1_0$ allow these vectors to be perpendicular to one another. For most defects symmetry also allows the third translation vector to be orthognal to the first two, creating an orthorhombic unit cell; however, as discussed below, this is not always optimal.

We use three additional criteria to construct unit cells that give an accurate defect energy for minimum N. Namely, the unit cells should (1) maintain maximum symmetry to reduce the number of k points, and be centered on an inversion point to eliminate symmetry-induced dipoles, (2) have defect planes separated by enough planes so that defect energies are converged, and (3) deviate slightly from being orthorhombic to reduce N.

The first point is useful to avoid constructing unit cells that may form a dipole moment, which makes both ASA and full-potential methods easier to converge. The second point is an issue of convergence: in real materials the defects are typically separated by many more planes than is possible in our calculations but we require only noninteracting defects. A carefully constructed nonorthorhombic cell, as recommended in point (3), can reduce N by up to a factor of 2 while keeping the total number of inequivalent atoms fixed, reducing computational cost but should be kept as close to orthorhombic as possible to keep numerical integrations well conditioned. This reduction in atoms/cell is possible in all cases except the CDB and the (001) and (110) APBs, which come in Co(Fe)- and Pt(Pd)-rich pairs at 50-50 stoichiometry.

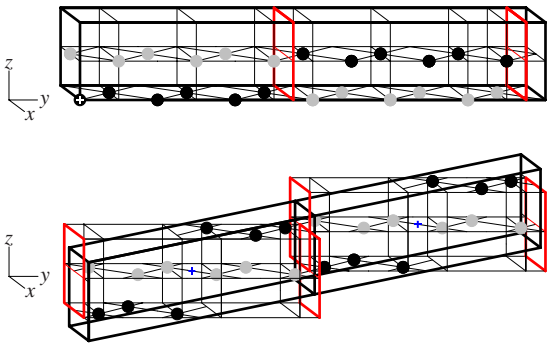

FIG. 7. (Color online) (Color online) (a) Orthorhombic cell with two (010) APBs. (b) Two alternative cells with one (010) APB each, with its origin at an inversion point. In both (a) and (b), the unit-cell boundaries are denoted by heavy black lines, the APBs by heavy red/gray lines. Other lines are provided to guide the eyes in identifying the $L1_0$ structure. The origin of each unit cell is denoted by a + symbol [white in (a), blue/gray in (b)]. Each cell in (b) has the same number of inequivalent atoms and atomic planes between defects as the cell in (a) but half the total atoms of (a).

To demonstrate, consider the cell in Fig. 7(a) that is orthorhombic and contains two defect planes, with its origin at the atom in the lower left corner (black atom with white "+"). In terms of a and c, the lattice vectors are $\{[a\ 0\ 0], [0\ 6a\ 0], [0\ 0\ c]\}$. Figure 7(b) shows two identical nonorthorhombic cells (lattice vectors $\{[a\ 0\ 0], [a/2\ 3a/2\ c/2], [0\ 0\ c]\}$), each with the same number of inequivalent atoms and number of planes between defects as in the orthorhombic cell [Fig. 7(a)] but with half as many defect planes and atoms per unit cell. The origin (blue/gray +) is placed at an inversion point, ensuring that there are no symmetry-induced dipoles.

APPENDIX B: SIZE OF THE ATOMS

Using SPR, the overlap of ASA spheres is consistently from 9.3–11.4 % in all cases. From the values of these radii (given below), one can notice that increase in the touching sphere radii to maintain volume conservation is done such that the smaller atoms expands more in comparison to the larger ones,[49] which minimizes the sphere-sphere overlap between two very differently sized atoms. Different sets of radii are found for A1 versus $L1_0$ because of configurational averaging, similar to CPA ideas.[49]

The touching MT-SPR for $L1_0$ CoPt are 1.3861 and 1.2908 Å (ratio 1.074) for Pt and Co, respectively. The ASA

radii are 1.5083 and 1.4475 Å (ratio 1.042), with a 10.4% overlap. The (011) CDB shows the defect energy minima at an ASA radii ratio very close to the undefected one. In contrast, the A1 MT-SPR radii for CoPt are 1.410 and 1.259 Å (ratio 1.120), and ASA radii of 1.520 and 1.454 Å (ratio 1.045), for an 11.4% overlap.

The MT-SPR in $L1_0$ FePd are 2.586 and 2.430 Å (ratio 1.064) for Pd and Fe, respectively, and the ASA radii are 2.834 and 2.694 Å (ratio 1.052), with a 10.2% overlap. The A1 MT-SPR radii were 2.563 and 2.443 Å (ratio 1.049), giving ASA radii of 2.827 and 2.720 Å (ratio 1.039) for Pd and Fe, respectively, with a 10.8% overlap.

Unlike the above two cases, the size difference between Fe and Pt in FePt is large and, hence, the importance of our optimal basis-set representation in this case is more pronounced. For $L1_0$ FePt, the touching MT-SPR are 2.718 and 2.339 Å (ratio 1.162) for Pt and Fe, respectively, giving rise to the corresponding ASA radii of 2.936 and 2.592 Å (ratio 1.133), with 9.3% overlap. The A1 MT-SPR are 2.635 and 2.342 Å (ratio 1.125), yielding ASA radii of 2.900 and 2.639 Å (ratio 1.099) for Pt and Fe, respectively, with a 11.3% overlap.

*duanej@illinois.edu

[1] K. R. Coffey, M. A. Parker, and J. K. Howard, IEEE Trans. Magn. **31**, 2737 (1995).
[2] R. A. Ristau, K. Barmak, L. H. Lewis, K. R. Coffey, and J. K. Howard, J. Appl. Phys. **86**, 4527 (1999).
[3] J. Penuelas, C. Andreazza-Vignolle, P. Andreazza, A. Ouerghi, and N. Bouet, Surf. Sci. **602**, 545 (2008).
[4] D. Alloyeau, C. Ricolleau, C. Mottet, T. Oikawa, C. Langlois, Y. Le Bouar, N. Braidy, and A. Loiseau, Nature Mater. **8**, 940 (2009).
[5] S. Sun, C. B. Murray, D. Weller, L. Folks, and A. Moser, Science **287**, 1989 (2000).
[6] N. I. Vlasova, G. S. Kandaurova, and N. N. Shchegoleva, J. Magn. Magn. Mater. **222**, 138 (2000).
[7] R. A. Lukaszew, A. Cebollada, C. Clavero, and J. M. Garcia-Martín, Physica B **384**, 15 (2006).
[8] B. Zhang and W. A. Soffa, IEEE Trans. Magn. **26**, 1388 (1990).
[9] V. V. Maykov, A. Y. Yermakov, G. V. Ivanov, V. I. Khrabrov, and L. M. Magat, Phys. Met. Metallogr. **67**, 76 (1989).
[10] J. Korringa, Physica (Utrecht) **13**, 392 (1947); W. Kohn and N. Rostoker, Phys. Rev. **94**, 1111 (1954).
[11] D. D. Johnson, A. Alam, and A. V. Smirnov, *MECCA: Multiple-scattering Electronic-structure Calculations for Complex Alloys (KKR-CPA Program, ver. 1.9)* (University of Illinois, Illinois, 2008).
[12] P. Soven, Phys. Rev. **156**, 809 (1967); D. W. Taylor, *ibid.* **156**, 1017 (1967).
[13] B. Zhang and W. A. Soffa, Phys. Status Solidi A **131**, 707 (1992).
[14] J. M. Sanchez, J. L. Moran-Lopez, C. Keroux, and M. C. Cadeville, J. Phys.: Condens. Matter **1**, 491 (1989).
[15] D. E. Laughlin, K. Srinivasan, M. Tanase, and L. Wang, Scr. Mater. **53**, 383 (2005).
[16] C.-B. Rong, D. Li, V. Nandwana, N. Poudyal, Y. Ding, and Z. L. Wang, Adv. Mater. **18**, 2984 (2006).
[17] A. G. Khachaturyan, *Theory of Structural Transformation in Solids* (Wiley, New York, 1983).
[18] I. M. Penisson, A. Bourret, and Ph. Eurin, Acta Metall. **19**, 1195 (1971); N. I. Vlasova, N. N. Shchegoleva, and Ya. S. Shur, Phys. Met. Metallogr. **58**, 43 (1984).
[19] N. I. Sokolovskaya, N. N. Shchegoleva, and G. S. Kandaurova, Phys. Met. Metallogr. **41**, 42 (1976).
[20] C. Leroux, Ph.D. dissertation, University of Strasbourg, 1989.
[21] Y. LeBouar, Ph.D. dissertation, Ecole Polytechnique, 1998.
[22] T. Klemmer, D. Hoydick, H. Okumura, B. Zhang, and W. A. Soffa, Scr. Metall. Mater. **33**, 1793 (1995).
[23] A. L. Roitburd, in *Phase Transformations '87*, edited by G. W. Lorimer (Institue of Metals, Cambridge, UK, 1988), p. 414.
[24] A. G. Khachaturyan, T. F. Lindsey, and J. W. Morris, Metall. Trans. A **19A**, 249 (1988).
[25] Q. F. Xiao, E. Brück, Z. D. Zhang, F. R. de Boer, and K. H. J. Buschowa, J. Alloys Compd. **364**, 64 (2004).
[26] C. Issro, M. Abes, W. Püschl, B. Sepiol, W. Pfeiler, P. F. Rogl, G. Schemerber, W. A. Soffa, R. Kozubski, and V. Pierron-Bohnes, Metall. Mater. Trans. A **37A**, 3415 (2006).
[27] J. B. Newkirk, R. Smoluchowski, A. H. Geisler, and D. L. Martin, J. Appl. Phys. **22**, 290 (1951).
[28] C. Leroux, A. Loiseau, D. Broddin, and G. Van Tandeloo, Philos. Mag. B **64**, 57 (1991).
[29] N. I. Vlasova, A. G. Popov, and N. N. Shchegoleva, Phys. Met. Metallogr. **107**, 359 (2009).
[30] Y. Le Bouar, A. Loiseau, and A. G. Khachaturyan, Acta Mater. **46**, 2777 (1998).
[31] M. E. Gruner, G. Rollmann, P. Entel, and M. Farle, Phys. Rev. Lett. **100**, 087203 (2008).
[32] M. E. Gruner and P. Entel, J. Phys.: Condens. Matter **21**, 293201 (2009).
[33] L.-L. Wang and D. D. Johnson, J. Am. Chem. Soc. **131**, 14023 (2009).
[34] G. Brown, B. Kraczek, A. Janotti, T. C. Schulthess, G. M. Stocks, and D. D. Johnson, Phys. Rev. B **68**, 052405 (2003).
[35] V. Crisan, P. Entel, H. Ebert, H. Akai, D. D. Johnson, and J. B. Staunton, Phys. Rev. B **66**, 014416 (2002).
[36] B. Yang, M. Asta, O. N. Mryasov, T. J. Klemmer, and R. W. Chantrell, Scr. Mater. **53**, 417 (2005).
[37] G. A. Held, H. Zeng, and S. Sun, J. Appl. Phys. **95**, 1481 (2004).
[38] D. D. Johnson, D. M. Nicholson, F. J. Pinski, B. L. Gyorffy, and G. M. Stocks, Phys. Rev. Lett. **56**, 2088 (1986).
[39] D. D. Johnson, D. M. Nicholson, F. J. Pinski, B. L. Gyorffy, and G. M. Stocks, Phys. Rev. B **41**, 9701 (1990).
[40] D. D. Johnson and F. J. Pinski, Phys. Rev. B **48**, 11553 (1993).
[41] D. D. Koelling and B. N. Harmon, J. Phys. C **10**, 3107 (1977).
[42] A. V. Smirnov, W. A. Shelton, and D. D. Johnson, Phys. Rev. B **71**, 064408 (2005).
[43] U. von Barth and L. Hedin, J. Phys. C **5**, 1629 (1972).
[44] V. L. Moruzzi, J. F. Janak, and A. R. Williams, *Calculated Elec-*

tronic Properties of Materials (Pergamon Press, New York, 1978).
[45] G. Voronoi, J. Reine Angew. Math. **134**, 198 (1908).
[46] O. K. Andersen, Phys. Rev. B **12**, 3060 (1975).
[47] P. Phariseau and W. M. Temmerman, *The Electronic Structure of Complex Systems* (Plenum, New York, 1984).
[48] H. J. Monkhorst and J. D. Pack, Phys. Rev. B **13**, 5188 (1976).
[49] A. Alam and D. D. Johnson, Phys. Rev. B **80**, 125123 (2009).
[50] D. Glötzel, B. Segall, and O. K. Andersen, Solid State Commun. **36**, 403 (1980); A. K. McMahan, Phys. Rev. B **30**, 5835 (1984); N. E. Christensen and S. Satpathy, Phys. Rev. Lett. **55**, 600 (1985).
[51] P. F. Zou and R. F. W. Bader, Acta Crystallogr., Sect. A: Found. Crystallogr. **50**, 714 (1994); R. F. W. Bader, *Theory of Atoms in Molecules* (Oxford University Press, Oxford, 1990).
[52] G. Kresse and J. Furthmuller, Phys. Rev. B **54**, 11169 (1996); Comput. Mater. Sci. **6**, 15 (1996).
[53] G. Kresse and D. Joubert, Phys. Rev. B **59**, 1758 (1999).
[54] C. S. Wang, B. M. Klein, and H. Krakauer, Phys. Rev. Lett. **54**, 1852 (1985).
[55] F. J. Pinski, J. B. Staunton, B. L. Gyorffy, D. D. Johnson, and G. M. Stocks, Phys. Rev. Lett. **56**, 2096 (1986).
[56] P. Bagno, O. Jepsen, and O. Gunnarsson, Phys. Rev. B **40**, 1997 (1989).
[57] D. J. Singh, W. E. Pickett, and H. Krakauer, Phys. Rev. B **43**, 11628 (1991).
[58] H. J. F. Jansen and S. S. Peng, Phys. Rev. B **37**, 2689 (1988).
[59] A. P. Sutton and R. W. Balluffi, *Interfaces in Crystalline Materials* (Clarendon Press, Oxford, 1995).
[60] D. D. Johnson, A. V. Smirnov, J. B. Staunton, F. J. Pinski, and W. A. Shelton, Phys. Rev. B **62**, R11917 (2000).
[61] F. Ducastelle, *Order and Phase Stability in Alloys* (North-Holland, The Netherlands, 1991).
[62] D. de Fontaine, Solid State Phys. **34**, 73 (1979).
[63] A. Khachaturyan, *Theory of Structural Transformations in Solids* (Wiley, New York, 1983).
[64] R. V. Chepulskii and W. H. Butler, Phys. Rev. B **72**, 134205 (2005).
[65] N. A. Zarkevich and D. D. Johnson, Phys. Rev. Lett. **92**, 255702 (2004).
[66] N. A. Zarkevich, T. L. Tan, and D. D. Johnson, Phys. Rev. B **75**, 104203 (2007).
[67] T. L. Tan, N. A. Zarkevich, and D. D. Johnson, Bull. Am. Phys. Soc. **52**, 6 (2007).
[68] C. Leroux, M. C. Cadville, V. Pierron-Bohnes, G. Inden, and F. Hinz, J. Phys. F: Met. Phys. **18**, 2033 (1988).
[69] *Binary Systems*, Landolt-Börnstein, New Series, Group IV, Physical Chemistry Vol. 5, Pt. E, edited by B. Predel (Springer-Verlag, Berlin, 2006).
[70] *Binary Systems*, Landolt-Börnstein, New Series, Group IV, Physical Chemistry Vol. IV, edited by H. Ullmaier (Springer-Verlag, Heidelberg, 1991).
[71] D. Paudyal, T. Saha-Dasgupta, and A. Mookerjee, J. Phys.: Condens. Matter **16**, 7247 (2004).
[72] R. Hayn and V. Drchal, Phys. Rev. B **58**, 4341 (1998).
[73] M. Müller, P. Erhart, and K. Albe, Phys. Rev. B **76**, 155412 (2007).
[74] Y. Chen, T. Atago, and T. Mohri, J. Phys.: Condens. Matter **14**, 1903 (2002).
[75] F. R. de Boer, R. Boom, W. C. M. Mattens, A. R. Miedema, and A. K. Niessen, *Cohesion in Metals: Transition Metal Alloys* (North-Holland, New York, 1988), Vol. 19.
[76] Y. Chen, S. Iwata, and T. Mohri, CALPHAD: Comput Coupling Phase Diagrams Thermochem. **26**, 583 (2002).
[77] R. Hultgren, P. D. Desai, D. T. Hawkins, M. Gleiser, and K. K. Kelley, *Selected Values of Thermodynamic Properties of Binary Alloys* (American Society for Metals, Metals Park, Ohio, 1973).
[78] P. Franke, D. Neuschütz, and Scientific Group Thermodata Europe, *Binary Systems*, Landolt-Börnstein, Group IV Vol. 19, Pt. B2 (Springer, Berlin, 2007).
[79] T. B. Massalski and H. Okamoto, *Binary Alloy Phase Diagrams* (ASM International, Materials Park, OH, 1996).
[80] H. Okamoto, J. Phase Equilib. **22**, 591 (2001).
[81] G. Ghosh, C. Kantner, and G. B. Olson, J. Phase Equilib. **20**, 295 (1999).
[82] H. Okamoto, *Binary Alloy Phase Diagrams*, 2nd ed., edited by T. B. Massalski (ASM International, Materials Park, OH, 1990), Vol. 2, pp. 1752–1756.
[83] K. Barmak, J. Kim, S. Shell, E. B. Svedberg, and J. K. Howard, Appl. Phys. Lett. **80**, 4268 (2002).
[84] J. M. MacLaren, R. R. Duplessis, R. A. Stern, and S. Willoughby, IEEE Trans. Magn. **41**, 4374 (2005).
[85] L. Wang, Z. Fan, A. G. Roy, and D. E. Laughlin, J. Appl. Phys. **95**, 7483 (2004).
[86] J. Lyubina, O. Isnard, O. Gutfleisch, K.-H. Müller, and L. Schultz, J. Appl. Phys. **100**, 094308 (2006).
[87] S. H. Whang, Q. Feng, and Y.-Q. Gao, Acta Mater. **46**, 6485 (1998).
[88] K. Barmak, J. Kim, L. H. Lewis, K. R. Coffee, M. F. Toney, A. J. Kellock, and J.-U. Thiele, J. Appl. Phys. **95**, 7501 (2004).
[89] J. M. MacLaren and R. H. Victora, J. Appl. Phys. **76**, 6069 (1994).
[90] H. Shima, K. Oikawa, A. Fujita, K. Fukamichi, K. Ishida, and A. Sakuma, Phys. Rev. B **70**, 224408 (2004).
[91] A. Kussmann, K. Müller, and Z. Agnew, Phys. **17**, 509 (1964).
[92] D. Weller and A. Moser, IEEE Trans. Magn. **35**, 4423 (1999).
[93] L. Petit, S. V. Beiden, W. M. Temmerman, Z. Szotek, G. M. Stocks, and G. A. Gehring, Philos. Mag. B **78**, 449 (1998); L. Petit, S. V. Beiden, W. M. Temmerman, G. M. Stocks, and G. A. Gehring, J. Phys.: Condens. Matter **12**, 8439 (2000).
[94] K. Sato, Y. Hirotsu, H. Mori, Z. Wang, and T. Hirayama, J. Appl. Phys. **98**, 024308 (2005).
[95] K. Sato, B. Bian, and Y. Hirotsu, J. Appl. Phys. **91**, 8516 (2002).
[96] H. Naganuma, K. Sato, and Y. Hirotsu, J. Magn. Magn. Mater. **310**, 2356 (2007).
[97] K. Binder, Physica (Amsterdam) **62**, 508 (1972).
[98] M. Farle, K. Baberschke, U. Stetter, A. Aspelmeier, and F. Gerhardter, Phys. Rev. B **47**, 11571 (1993).
[99] F. J. Pinski, B. Ginatempo, D. D. Johnson, J. B. Staunton, G. M. Stocks, and B. L. Gyorffy, Phys. Rev. Lett. **68**, 1962 (1992).
[100] W. Grange, I. Galanakis, M. Alouani, M. Maret, J.-P. Kappler, and A. Rogalev, Phys. Rev. B **62**, 1157 (2000).
[101] P. Kamp, A. Marty, B. Gilles, R. Hoffmann, S. Marchesini, M. Belakhovsky, C. Boeglin, H. A. D'urr, S. S. Dhesi, G. van der Laan, and A. Rogalev, Phys. Rev. B **59**, 1105 (1999).
[102] P. Villars and L. D. Calvert, *Pearson's Handbook of Crystallographic Data for Intermetallic Phases* (American Society of Metals, Metals Park, OH, 1985).
[103] I. Galanakis, M. Alouani, and H. Dreysse, Phys. Rev. B **62**, 6475 (2000).

[104] A. Kootte, C. Haas, and R. A. de Groot, J. Phys.: Condens. Matter **3**, 1133 (1991).
[105] I. Osterloh, P. N. Oppeneer, J. Sticht, and J. Kubler, J. Phys.: Condens. Matter **6**, 285 (1994).
[106] K. D. Belashchenko and V. P. Antropov, J. Magn. Magn. Mater. **253**, 87 (2002).
[107] T. J. Klemmer, C. Liu, N. Shukla, X. W. Wu, D. Weller, M. Tanaseb, D. E. Laughlin, and W. A. Soffa, J. Magn. Magn. Mater. **266**, 79 (2003).
[108] Z. R. Dai, S. Sun, and Z. L. Wang, Nano Lett. **1**, 443 (2001).
[109] A. J. Lapworth and J. P. Jakubovics, Philos. Mag. **29**, 253 (1974).